Original Article

Microstructure, mechanical properties and machinability of particulate reinforced Al matrix composites: a comparative study between SiC particles and high-entropy alloy particles

Tiwen Lu [a,b], Tianbing He [b], Zixuan Li [a], Hongyu Chen [b], Xiaoliang Han [b], Zhiqiang Fu [a,*], Weiping Chen [a,*]

[a] Guangdong Key Laboratory for Advanced Metallic Materials Processing, South China University of Technology, Guangzhou, Guangdong 510640, China

[b] IFW Dresden, Institute for Complex Materials, Helmholtzstraße 20, D-01069 Dresden, Germany

ARTICLE INFO

ABSTRACT

In this study, 2024Al matrix composites reinforced by SiC particles (SiC-2024Al) and nanocrystalline high-entropy alloy particles (HEA-2024Al) fabricated by powder metallurgy were systematically compared for the first time. There is a significant difference in microstructure and mechanical properties as well as machinability between two kinds of composites. In term of microstructure, when the volume fraction of reinforcements was 10%, both SiC-2024Al and HEA-2024Al composites showed a homogeneous particle distribution in the matrix. With the increase of reinforcement content, HEA-2024Al composites presented denser microstructure than that of SiC-2024Al composites. The composites with 10, 20 and 30 vol.% HEA reinforcements all showed better plasticity than that of the SiC-2024Al composites with same volume fraction of reinforcements, which was related with better particle distribution and interface bonding. However, the strength showed the opposite tendency in the two kinds of composites. Selecting 10SiC-2024Al and 10HEA-2024Al composites as examples to explore the difference in the yield strength of two kinds of composites, it is ascribed to the dislocation punched zones around interface between the Al matrix and reinforcements, which was analyzed in detail by a combination of calculation, nanoindentation tests and finite element analysis. Additionally, HEA-2024Al composites showed better machinability than those of SiC-2024Al composites. This work provides insight into the application of particulate reinforced Al matrix composites.

* Corresponding authors.
E-mails: kopyhit@163.com (Z. Fu), mewpchen@scut.edu.cn (W. Chen).

1.   Introduction

Aluminum matrix composites (AMCs) are widely used in various engineering applications [1,2]. Among them, ceramic particulate reinforced aluminum matrix composites are one of the most promising engineering materials, ascribed to their outstanding thermal properties, mechanical properties and cost effectiveness [3–5]. Due to the addition of hard ceramic particles, the modulus and strength are significantly improved. However, ceramic particles are harder and stiffer than the matrix, resulting in results that machining becomes more difficult than that of conventional materials [3]. Some researchers [6] mentioned that adding high-stiffness ceramic whiskers into the ductile matrix resulted in thermal mismatch and plastic incompatibility, severely decreased the forgeability of the composite. How to improve the machinability of composites is always a tough task [6–9]. Due to the high cost of polycrystalline diamond (PCD) tools [7], generally, there is a clear and tangible demand for cheaper and efficient turning of MMCs. Additionally, many researches show that both extrinsic (cutting speed, feed rate, depth of cut and type of cutting tools) and intrinsic (particulate size, volume fraction) parameters affects machinability of particle reinforced MMCs [7–9]. Among all parameters, the type of reinforcement is one of important factors.

Good mechanical properties can also be achieved when metallic particles are introduced into Al matrices. This is mainly due to the stable metallurgical bonding formed at the interface between the Al matrix and metallic particles, and adequate load bearing ability of metallic particles [10–12]. High-entropy alloy (HEA) particles have been one of the most frequently used reinforcements by powder metallurgy, squeeze casting and friction stir processing (FSP) [13–16]. Meng et al. [13] prepared AlCoCrCuFeNi high-entropy alloy particle reinforced magnesium matrix composite by laser melt injection on the surface of magnesium alloy, and the wear of 40 vol.% high entropy alloy particle reinforced magnesium matrix composite coating was only one seventh of the matrix. Yang et al. [14] added AlCoCrCuFeNi high-entropy particles to the AA5083 matrix by using the underwater friction stir processing, and found that the grains of the prepared composite were obviously refined to obtain better strength and plasticity. Nanocrystalline high-entropy alloy (NC-HEA) particles can be prepared by mechanical alloying, and keep good thermal stability during the processing [15,16]. More importantly, due to the addition of NC-HEA$_p$, the composites show improved strength and balanced plasticity [15]. However, it is a short time when researchers used the metallic particles as the reinforcements, and no work has been done about the machinability of composites reinforced by metallic particles. There is also few literature about comparisons between composites reinforced with ceramic particles and composites reinforced metallic particles. Selvakumar et al. compared Mo$_p$/6082Al [17] and TiC$_p$/6082Al [18] composites in mechanical properties, Mo$_p$/6082Al composites displaying better elongation than that of TiC$_p$/6082Al composites. However, the comparison mentioned above is based on the different process methods.

In view of above discussions, this work was motivated by the following factors: firstly, the comparisons between composites reinforced with ceramic particles and composites reinforced with metallic particles have rarely been studied. Secondly, whether the machinability of composites can be improved by using metallic particles to replace ceramic particles. To explore the two aspects, silicon carbide (SiC) and nanocrystalline high-entropy alloy (NC-HEA) particles were selected as the reinforcements. 10 vol.%, 20 vol.% and 30 vol.% particulate reinforced 2024Al matrix composites have been well prepared to study the difference in microstructure, mechanical properties and machinability of two kinds of composites.

2.   Experimental

2.1.   Materials preparation

The irregular SiC particle with an average diameter of 14.7 mm, supplied by ChaoXing Nanotechnology Co., Ltd. China, was selected as the reinforcement. The other reinforcement, nanocrystalline CoNiFeCrAl$_{0.6}$Ti$_{0.4}$ high-entropy alloy particle, was synthesized by ball milling mixtures of Al, Fe, Ni, Co, Cr and Ti elemental powders (purity higher than 99.6 wt.%) for 60 h at a speed of 320 rpm with process control agent of cyclohexane, which were dried in vacuum chamber. The size of final NC-HEA powders was controlled less than 25 μm (500 mesh). The specific preparation process has been widely described in our previous work [15]. The reinforcement shape was not taken in account in this work. Gas-atomized 2024Al powders were used as the matrix. The morphology and size distribution of the above powders are shown in Fig. 1. The two reinforcements were mixed with the 2024Al powders and subsequently milled at a speed of 200 rpm with a ball-to-powder weight ratio of 10:1 for 10 h, respectively. The ball milling experiments were carried out in a high energy planetary ball mill (QM-3SP2 Planetary Ball Mill). A vacuum hot pressing device (HP-12 × 12 × 12, Centorr Vacuum Industries, USA) was utilized to sinter the composite powders at 480 °C for 0.5 h with a pressure of 150 MPa, and subsequently the bulk composites were hot extruded at 450 °C with an extrusion ratio of 10:1. Al matrix composites with 10 vol.%, 20 vol.% and 30 vol.% of reinforcements were successfully fabricated (hereafter named 10HEA-2024Al, 20HEA-2024Al, 30HEA-2024Al; 10SiC-2024Al, 20SiC-2024Al, 30SiC-2024Al, respectively).

2.2.   Materials characterization

The size distribution of the powders was characterized using a Mastersizer 2000 laser diffraction system (Malvern, UK). The microstructure of the composites was characterized by scanning electron microscopy (SEM, NOVA NanoSEM 430, USA) and high resolution transmission electron microscopy (HRTEM, G2 F20) equipped with an energy dispersive spectrometer (EDS). TEM specimens were firstly polished to ~50 μm and then thinned to electron transparency by ion milling. The nanoindentation measurements were done by a Hysitron TI-950 equipped with a standard Berkovich diamond indenter tip, in the load-controlled mode. Prior to the nanoindentation tests, the specimen surface was carefully prepared using metallographic techniques and subsequently polished with firstly
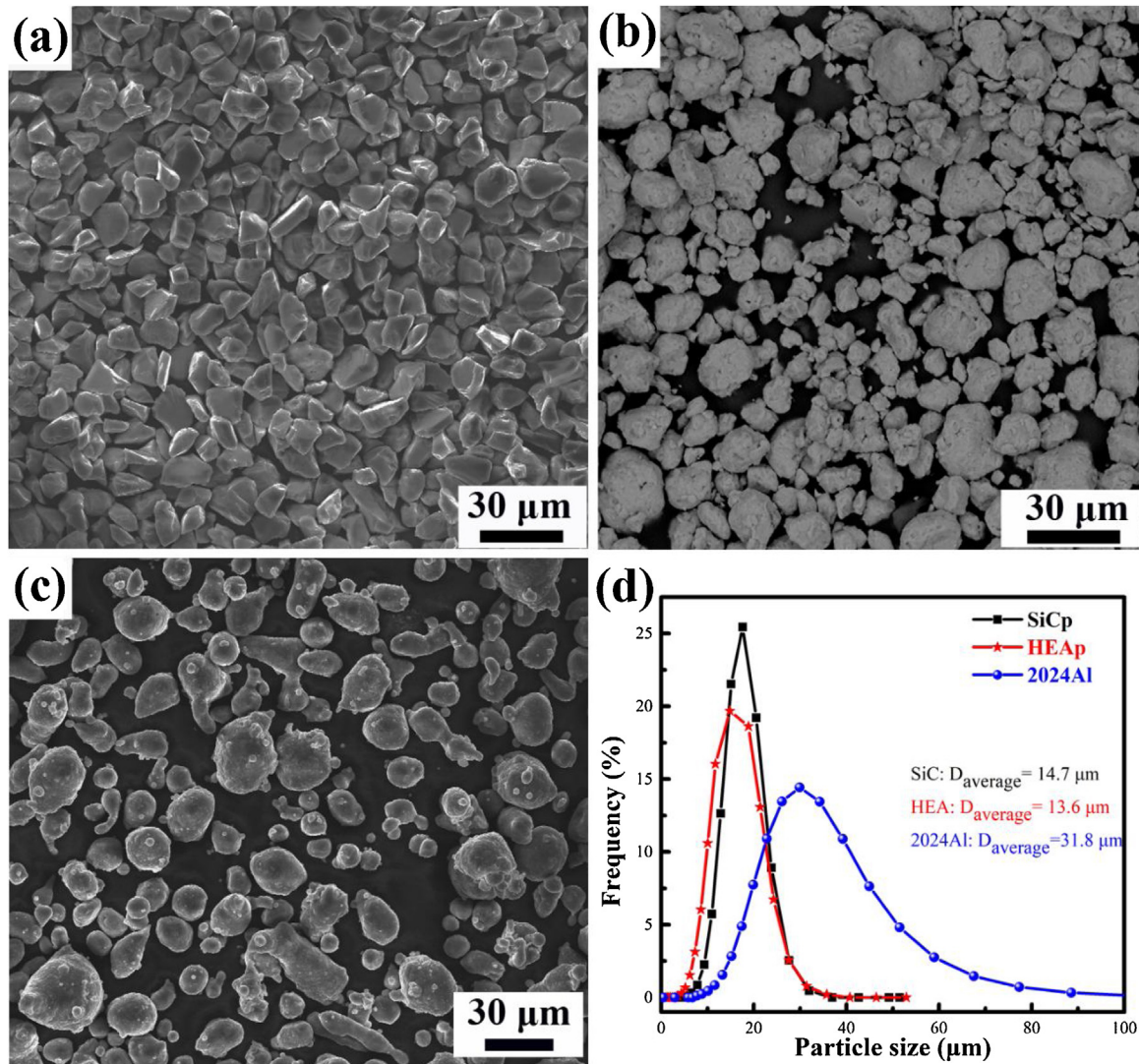
Fig. 1 – Morphology and size distribution of powders: (a) SiC; (b) HEA; (c) 2024Al; (d) particle size distribution.

2.5 μm, 1 μm and then 0.25 μm diamond abrasive for 20 min. A 1 μm spacing between neighboring indents and a 500 μN maximum indentation load were used in the following experiments. Both tensile tests (the cylindrical specimens with a 15 mm gauge length and 3 mm in diameter) and compression tests (Φ3 mm × 4.5 mm) were conducted using an INSTRON 5869 testing system (USA, INSTRON) at a speed of $5 \times 10^{-3}\,s^{-1}$ and $1 \times 10^{-3}\,s^{-1}$, respectively.

2.3. Machinability tests

The turning experiments were carried out on a CNC CA6150i lathe (DMTG Co., China) under dry condition without lubricant and coolant. The cemented carbide inserts (YBC251/TNMG160404-PM) were embedded in the tool substrate. Turning experiments was conducted with a cutting speed of 10 m/min, feed rate of 0.1 mm/r and a depth-of-cut of 0.05 mm. For the same cutting parameter, every insert was taken down from the tool substrate after the cylindrical samples (φ20 mm × 30 mm) machined with a length of 10 mm,

respectively. Then, the inserts were cleaned in alcohol (99%) by ultrasonic. The wear morphologies of inserts and chips were observed by SEM.

3. Results

3.1. Microstructure

Fig. 2 is the polished cross-section of the as-extruded composites as a function of the volume fraction of reinforcements. In term of SiC-2024Al composites, the 10SiC-2024Al composite shows a uniform distribution of SiC particles in the matrix. However, some particle agglomeration (red dashed circles) and pores (black arrows) can be found in the 20SiC-2024Al and 30SiC-2024Al composite. Experiments show that non-uniformity arises when the content of the SiC particulate reinforcement increases. All HEA-2024Al composites show denser microstructure than those of SiC-2024Al composites, which is related with the characteristic that HEA particles have more deformability than that of SiC particles during the
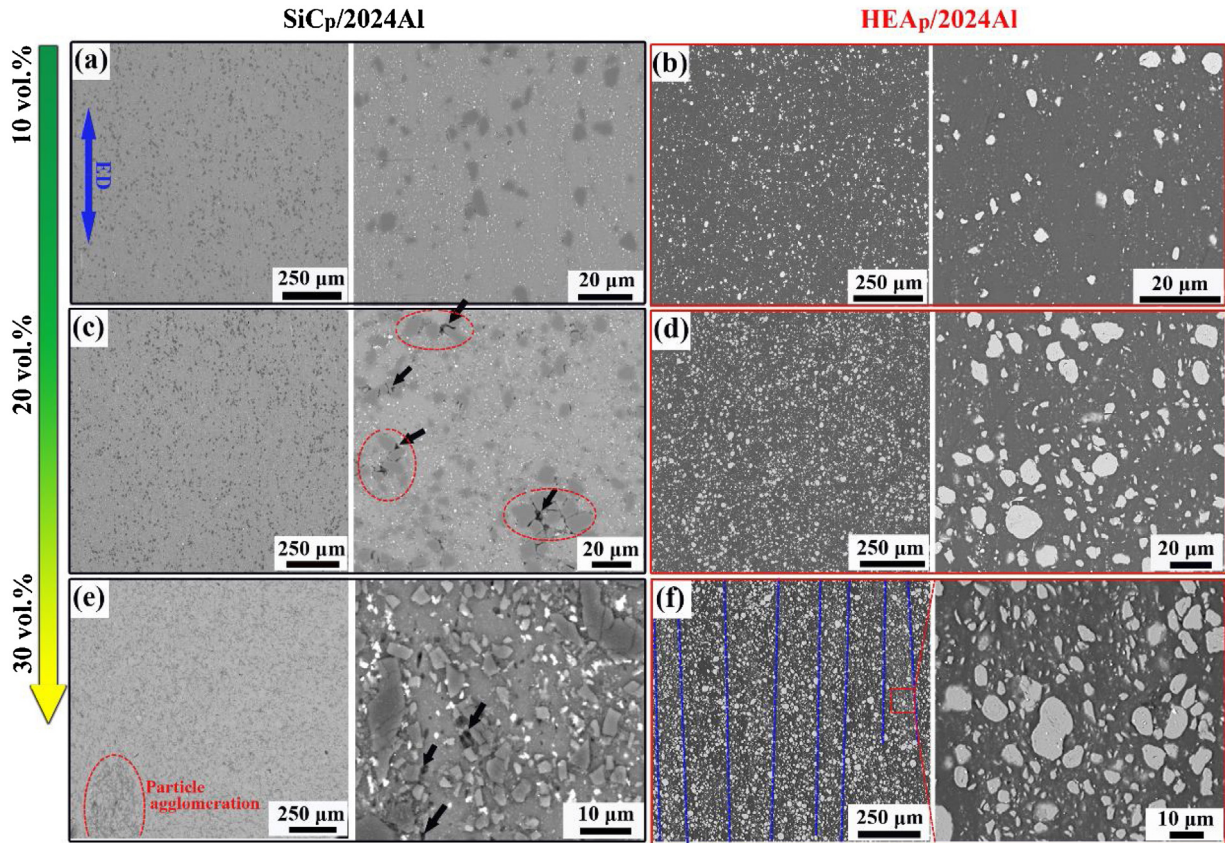
Fig. 2 – SEM images of hot extruded composites along the extrusion direction (ED): (a, c, e) 10SiC-2024Al, 20SiC-2024Al and 30SiC-2024Al composites, respectively; (b, d, f) 10HEA-2024Al, 20HEA-2024Al and 30HEA-2024Al composites, respectively.
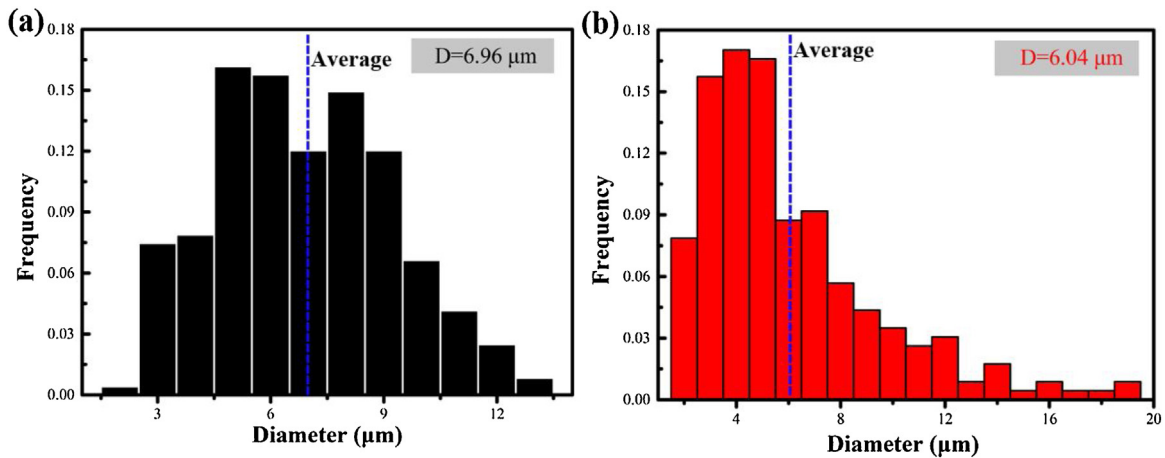

Fig. 3 – The distribution of reinforcement size in as-extruded composites: (a) 10SiC-2024Al composite, (b) 10HEA-2024Al composite.

hot pressing and hot extrusion. The 30HEA-2024Al composite presents some layered structures made up of sub-micron HEA particles. Our former results reported that the hierarchical microstructure has been found in the HEA-2024Al composite powder, which displayed a core consisting of relatively large HEA particles embedded in the Al matrix and a shell composed of many fine HEA particles [15]. When the fraction volume of HEA particles reaches 30 vol.%, the core–shell structure might be finally transformed into layered structures

after the hot pressing and hot extrusion. Notably, particle size statistics based on SEM images, the average particle sizes of 10SiC-2024Al and 10HEA-2024Al composites are 6.96 μm and 6.04 μm (Fig. 3), respectively, which indicates that there is still no obvious difference in two reinforcement particle size after ball milling. Fig. 4 shows XRD patterns of the composites. It can be seen that there are the Al, Al_2Cu and Al_7Cu_2Fe in both composites. The Al_2Cu phase was normally formed during the hot pressing [19]. Notably, the intensity of Al_2Cu in the SiC-2024Al
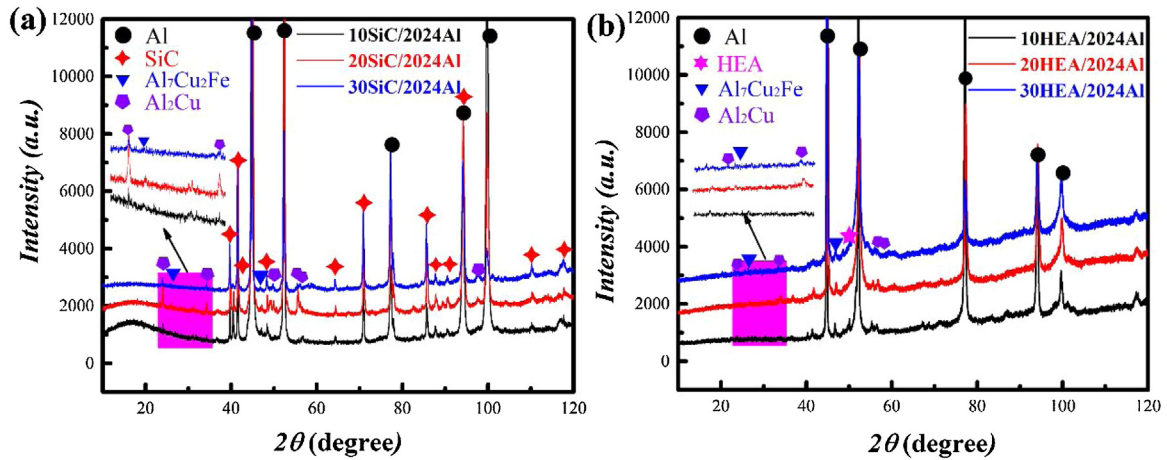
Fig. 4 – XRD patterns of as-extruded composites: (a) SiC particle reinforced Al matrix composites, (b) HEA particle reinforced Al matrix composites.
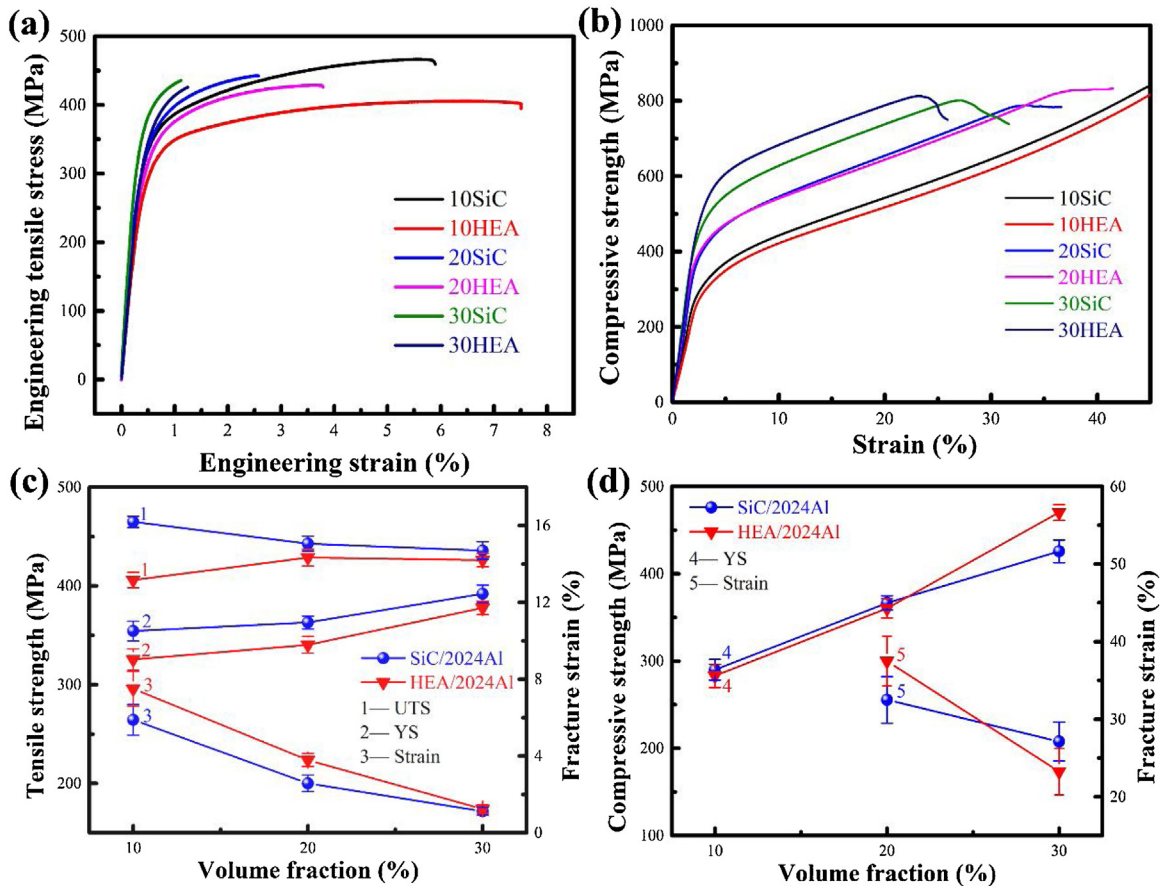

Fig. 5 – Mechanical properties of two kinds of hot extruded composites: (a) engineering tensile stress-strain curves; (b) engineering compressive stress-strain curves; (c) comparisons of ultimate tensile strength (UTS), yield strength (YS) and fracture strain; (d) comparisons of compressive yield strength and strain.

composites is significantly higher than that of the HEA-2024Al composites.

3.2. Mechanical properties

Figs. 5(a) and (c) show the engineering tensile properties of two kinds of composites. With the increase of rein-

forcement content, the yield strength and fracture strain of two kinds of composites display increased and decreased tendency, respectively. It is worth mentioning that all SiC-2024Al composites show higher tensile strength than those of HEA-2024Al composites with same volume fraction of reinforcement, whereas the fracture strain shows the opposite
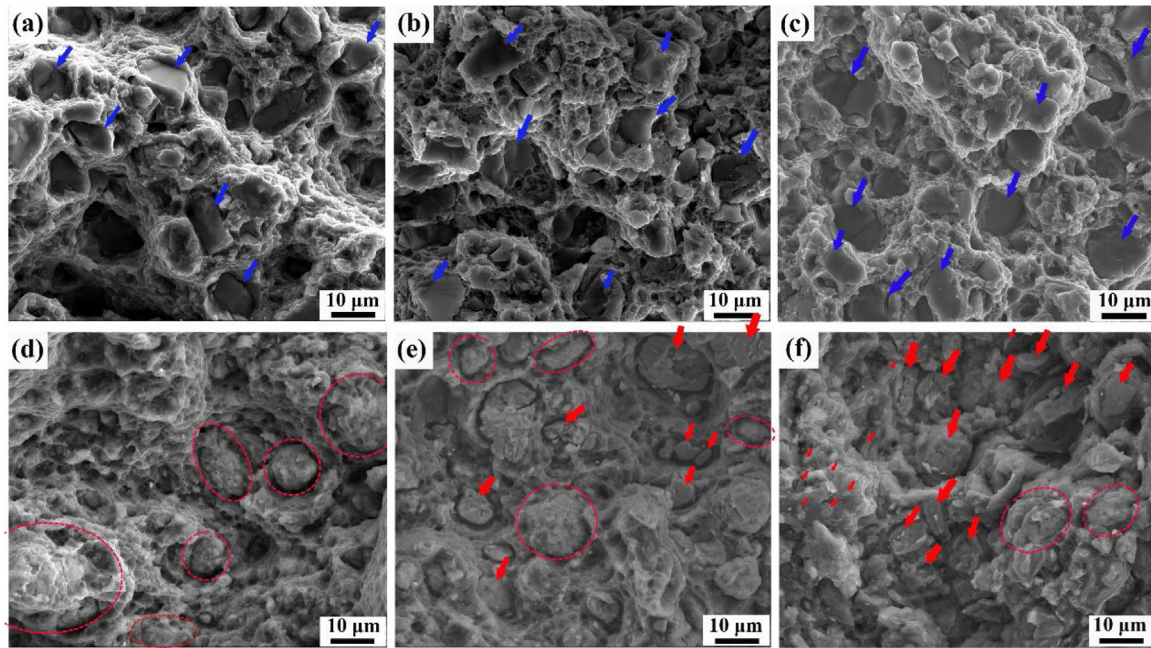
Fig. 6 – SEM images showing the fracture surfaces of two kinds of composites with the different reinforcement content: (a) 10SiC-2024Al composite, (b) 20SiC-2024Al composite, (c) 30SiC-2024Al composite, (d) 10HEA-2024Al composite, (e) 20HEA-2024Al composite, (f) 30HEA-2024Al composite.

tendency. The ultimate tensile strength in SiC-2024Al composites decreases with the increase of the reinforcement content, which might be ascribed to defects and particle aggregations. Tension–compression (T/C) asymmetry is controversial in Al matrix composites reinforced by metallic particles [12,13]. Therefore, the compressive properties of composites are measured, shown in Fig. 5(b) and (d). The overall tendency in the yield strength is consistent with tensile properties, except for two composites reinforced with 30 vol.% reinforcements. The layered structure in the 30HEA-2024Al composite is the reason for higher compressive yield strength than that of the 30SiC-2024Al composite.

3.3. Fracture morphology

For the tensile fracture of SiC-2024Al composites (Fig. 6(a)–(c)), all of them show fractured SiC particles, marked by blue arrows, similar with reports in former work [20,21]. Fractured SiC particles are mainly ascribed to residual stress in the SiC particle due to its coefficient of thermal expansion (CTE) far different from that of the matrix [21]. However, in the 10HEA-2024Al composite, interface debonding between the Al matrix and HEA particles is the main characteristic (Fig. 6(d)). Besides, the surfaces of HEA particles have some matrix dimples, which is related with good interface bonding and high-strength nanocrystalline HEA particles [15]. Increasing the HEA content, however, the composites present a larger ratio of fractured HEA particles (marked by red arrows in Fig. 6(e) and (f)), which is attributed to nonhomogeneous particle distribution resulting in stress concentration around HEA reinforcements [11]. Fig. 7 shows the lateral surface of the compressed composite samples after polishing. Because of the

good ductility, both the 10SiC-2024Al and 10HEA-2024Al composites have no cracks in the samples after a 50% deformation. There are two cracks in the 20SiC-2024Al composite along the diagonal direction, while only one crack near the surface of 20HEA-2024Al sample can be found, which can illustrate that the ductility of the latter is better than the former. There are two long cracks in the 30SiC-2024Al composite along the diagonal direction, and there are also three short cracks present in the 30HEA-2024Al composite. It is worth mentioning that the cracks in the 30HEA-2024Al composite seem to originate from the layered structure (inset in Fig. 7(f)), which indicates that the layered structure in the 30HEA-2024Al composite is harmful for the ductility of composites.

3.4. Crack propagation

In order to investigate concrete factors affecting the mechanical behavior in the SiC-2024Al and HEA-2024Al composites, crack propagation paths were obtained in the compressive tests of 20SiC-2024Al and 20HEA-2024Al composites, shown in the SEM images (Fig. 8). Evidently, the crack propagation paths exhibit significant difference in the two composites. In the SiC-2024Al composite, SiC particles show obvious interfacial debonding with the matrix along the crack (Fig. 13(a)), and there is no matrix attached to the surfaces of SiC particles. Besides, many fractured SiC particles (marked by blue arrows) can also be seen on both sides of the crack. In contrast, the crack deflects when it encounters HEA particles in the 20HEA-2024Al composite, shown in Fig.13(b), which indicates that the HEA particles can hinder the crack propagation and raise the damage tolerance of HEA/2024Al composites. Along the cracks, fractured HEA particles are hardly seen, and
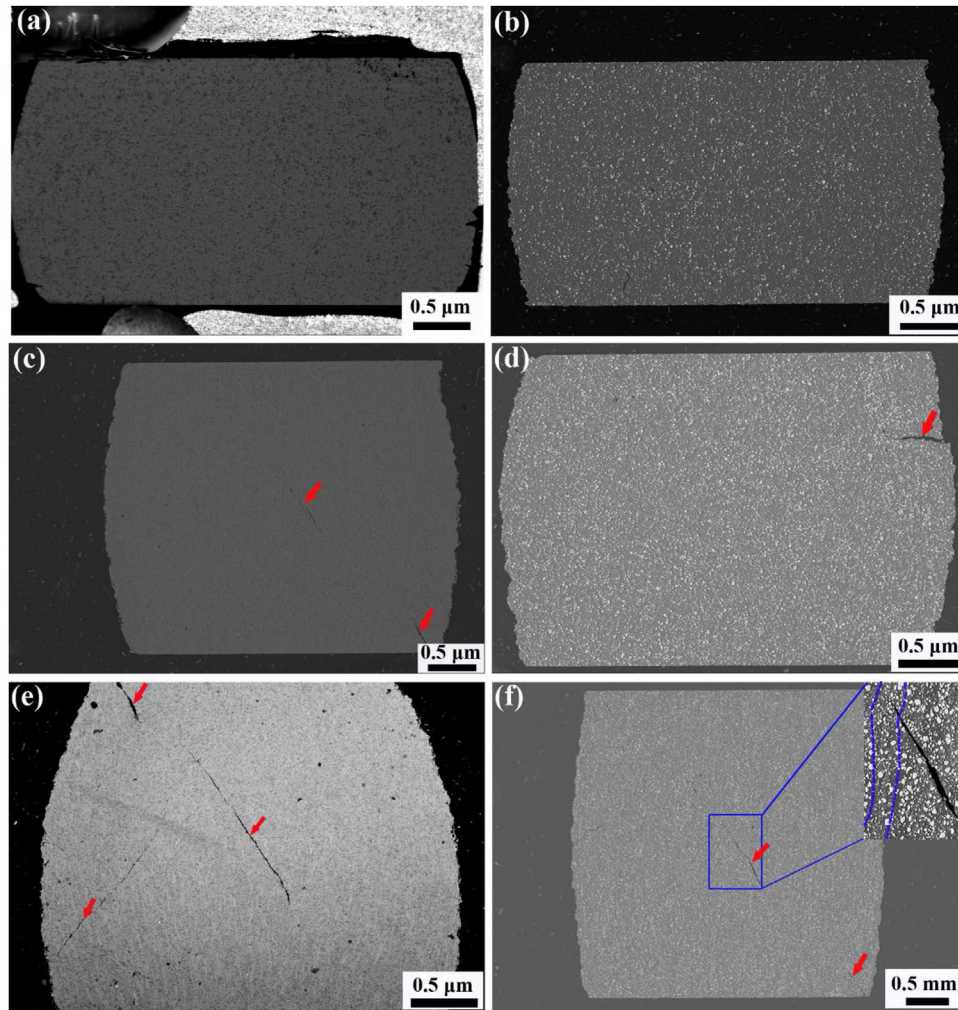
Fig. 7 – The cross-section of composites after compression tests: (a) 10SiC-2024Al composite, (b) 10HEA-2024Al composite, (c) 20SiC-2024Al composite, (d) 20HEA-2024Al composite, (e) 30SiC-2024Al composite, (f) 30HEA-2024Al composite.

some matrix can be seen on the surface of HEA particles. The further observation reveals that the crack propagation path in the 20HEA-2024Al composite has a more winding shape in comparison to that in the 20SiC-2024Al composite. Based on the above observations, it can be concluded that the interface structure in HEA/2024Al composites is better than that of SiC/2024Al composites, supporting the better plasticity of HEA/2024Al composites.

3.5. Machinability

Fig. 9 presents the surfaces of hot extruded composite bars. When the volume fraction of reinforcements reaches 10%, both surfaces of the two kinds of composites are smooth. 20HEA-2024Al and 30HEA-2024Al composites also show good surfaces. However, there are many cracks on the surfaces of both 20SiC-2024Al and 30SiC-2024Al composites, and with the increase of volume fraction, the condition become worse. Because the properties of the SiC particle have a huge difference with that of the Al matrix, the hot deformation behavior of the SiC/Al composite is different from that of traditional metallic materials. Adding high-hardness SiC particles into

the ductile matrix increases the resistance to hot plastic deformation and then brings the risk of damage during hot working. The higher the volume fraction of SiC particles is, the worse the deformability of composites is. Fig. 10 shows the comparison in machinability between SiC-2024Al and HEA-2024Al composites. Fig. 10(a) presents the schematic diagram of dry turning experiments. Reinforcement types have a significant influence on the machined surface of materials. As shown in Fig. 10(b), with increasing the volume fraction, composites reinforced by SiC particles break off at the middle and edge of the workpieces due to the presence of hard abrasive particles and the high pressure generated at the cutting zone. By contrast, the surfaces of three HEA-2024Al composites are flat and smooth. From the images of flank faces of tools after turning experiments in Fig. 10(c), the tool wear of SiC-2024Al composites is significantly severer than that of HEA-2024Al composites. Besides, worn areas of tools used in SiC-2024Al composites increase with the increase of the reinforcement content. There are limited tool wear in the HEA-2024Al composites with different reinforcement content. Shown in Fig. 10(d), short C-type chips were formed as observed in the 10SiC-2024Al composite and 20SiC-2024Al
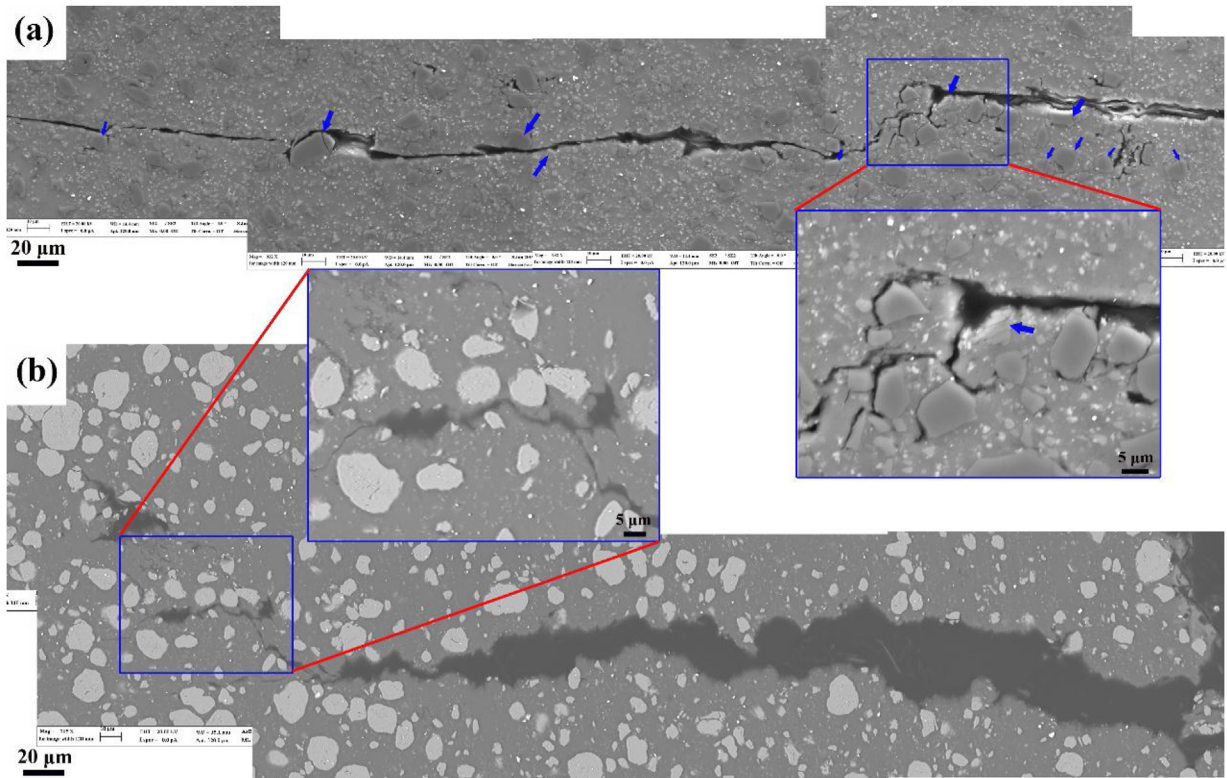
Fig. 8 – Crack propagation paths in the two composites based on compressive tests: (a) the 20SiC-2024Al composite, (b) the 20HEA-2024Al composite.

composite. Many bulk chips are found in the 30SiC-2024Al composite, which ascribed to the 30SiC-2024Al composite containing higher amount of hard and wear-resistant particles, difficult for turning. Long spring-type chips were obtained in the 10HEA-2024Al, and short ear-type chips were produced during the turning of 20HEA-2024Al and 30HEA-2024Al composites. Prior studies discussed the effect of machining conditions on chip formation for metal-matrix composites [22], which demonstrated that the increased volume fraction of hard reinforcements reduced ductility of the composites, and the composites favored chip breakage when compared to the machining of the matrix. Generally speaking, HEA-2024Al composites have better machinability than SiC-2024Al composites.

3.6. TEM observations

To explore the difference in mechanical properties between SiC-2024Al and HEA-2024Al composites, grain size and interface structure were observed using TEM (Figs. 11 and 12). Fig. 11(a)–(d) show the shape and size distribution of grains in 10SiC-2024Al, 10HEA-2024Al, 20SiC-2024Al and 20HEA-2024Al composites, respectively. Based on about 300 grains, it is found that the grain size of composites with the same reinforcement content is close. When the volume fraction of reinforcements increases from 10 vol.% to 20 vol.%, the grain size of composites almost falls by half. Fig. 11(e)–(h) display microstructure around reinforcements in these four composites, and dislocation zones can be easily observed around the SiC$_p$/Al interface
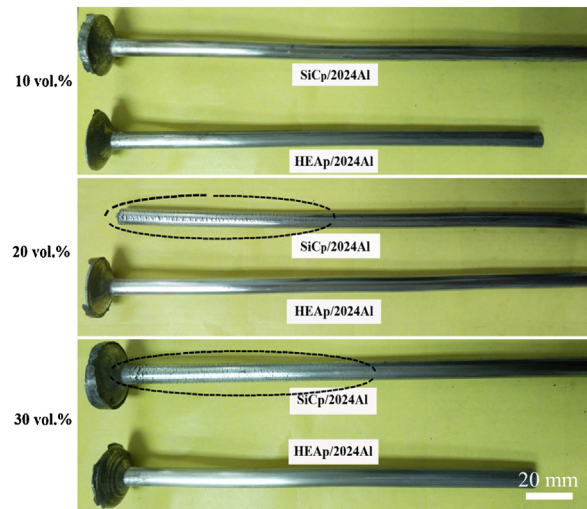

Fig. 9 – The surfaces of hot extruded composite bars.

in the SiC-2024Al composites (Fig. 11(e) and (g)). Besides, the length of dislocation zones increase with increasing the reinforcement content. As the micro-zone of the HEA-2024Al composite shown in Fig. 10(f) and (h), the dislocation density around the interface between the Al matrix and HEA particles is relatively low. This behavior is related with the smaller CTE difference between the Al matrix and HEA particles than that between the Al matrix and SiC particles. Additionally, HEA particles possess the better damage tolerance and
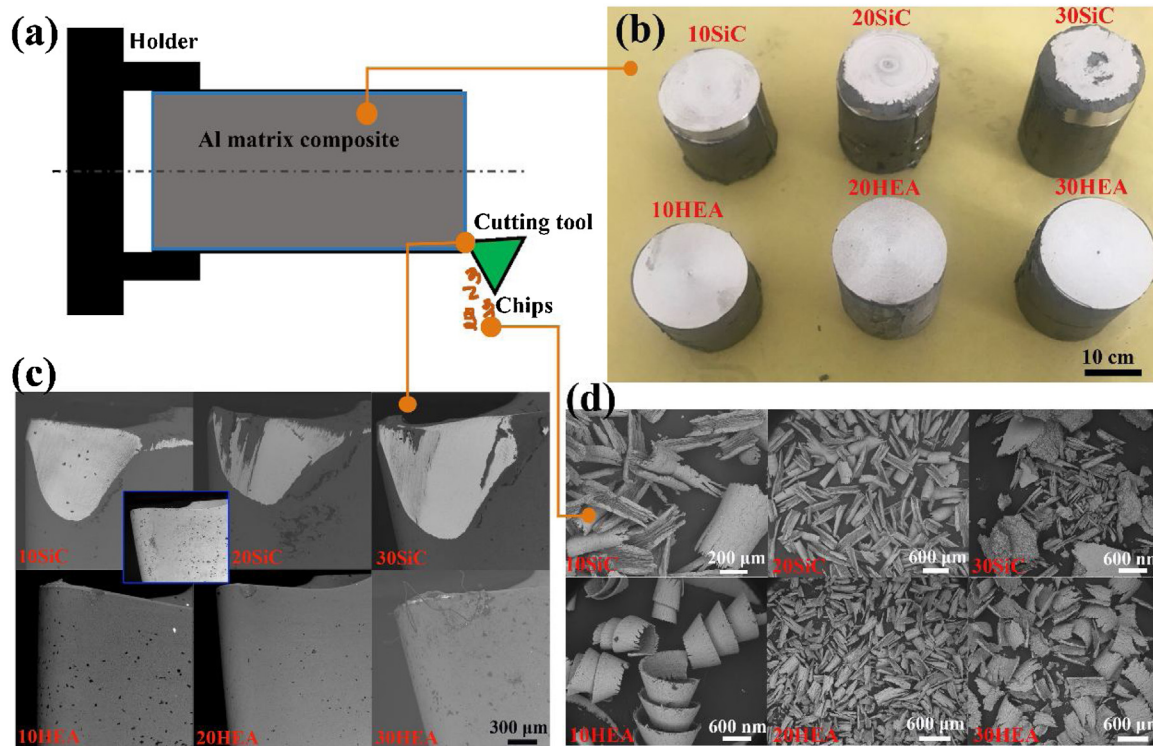
Fig. 10 – The comparison in machinability between SiC-2024Al and HEA-2024Al composites: (a) schematic diagram of dry turning experiments, (b) the surface condition of composites after machining, (c) SEM images of flank faces of cutting tools after the turning experiments (inset is original condition), (d) chips of different composites.

fracture toughness than those of SiC particles [14]. Selecting 10SiC-2024Al and 10HEA-2024Al composites as examples to investigate the interface in two kinds of composites, the interface length and interface structure are also completely different. Observed from the line scanning in Fig.12, only a thin oxide layer can be seen in the interface between the Al matrix and SiC_p, while a 200 nm interfacial layer contains Al, Cu, Co and Ni aggregation between the Al matrix and HEA. Interface consumes some Cu, leading to the result that the density of the Al_2Cu phase in HEA-2024Al composites is relatively lower than that of SiC-2024Al composites, which were verified by the XRD patterns (Fig. 4).

3.7. Hardness variation in the vicinity of interface

In the former literature [23,24], the measured hardness is dependent on the grain size and grain orientations to some extent. Therefore, several arrays of indentation points in random direction were normally conducted. Selecting 10HEA-2024Al and 10SiC-2024Al composites as examples, at least 3 arrays of indentation across interface were operated, and 20 individual indents for each indentation array were performed, shown in Fig. 13(a) and (d). Fig. 13(b) and (e) show the distribution of hardness and reduced modulus across the interface of composites. The red dashed lines corresponds to the approximate position of the interface in Fig. 12(b) and (d), the right of which corresponds to the Al matrix, and the left of which represents the reinforcements. In the Fig. 12(b), in the left of interface, the plateau has the magnitude of

~28 GPa and ~10 GPa, corresponding to the hardness of the SiC_p and HEA_p, respectively. In the left regime, there are two distinct regions, which shows different hardness values reduction from the interface to the Al matrix in the two composites. Regarding the 10SiC-2024Al composite, the hardness generally shows a gradual reduction from the interface to the Al matrix, and the width of this transition region is about 3 μm. When the indentations are more than 3 μm away from the SiC/Al interface, the hardness values reach a plateau of ~2 GPa. However, for the 10HEA-2024Al composite, the transition zone is not obvious, and the width may be smaller than 2 μm. The variation of reduced modulus is similar with that of hardness values, shown in Fig. 12(e). The fluctuations of the hardness around the interface is due to the presence of dislocations, demonstrating that the larger punched zones exist in SiC/2024A composites, which is one of reasons for the higher yield strength of 10SiC-2024Al composite than that of the 10HEA-2024Al composite [25]. Fig. 13(c) and (f) display typical load-displacement curves of the reinforcement, transition region and matrix in 10SiC-2024Al and 10HEA-2024Al composites.

4. Discussion

The strength increment in these composites can be explained by several contributions: Hall-Petch strengthening (σ_{H-P}), load transfer effect (σ_{L-T}), Orowan strengthening ($\Delta\sigma_{Or}$), as well as geometrically necessary dislocation strengthening ($\Delta\sigma_{GND}$)
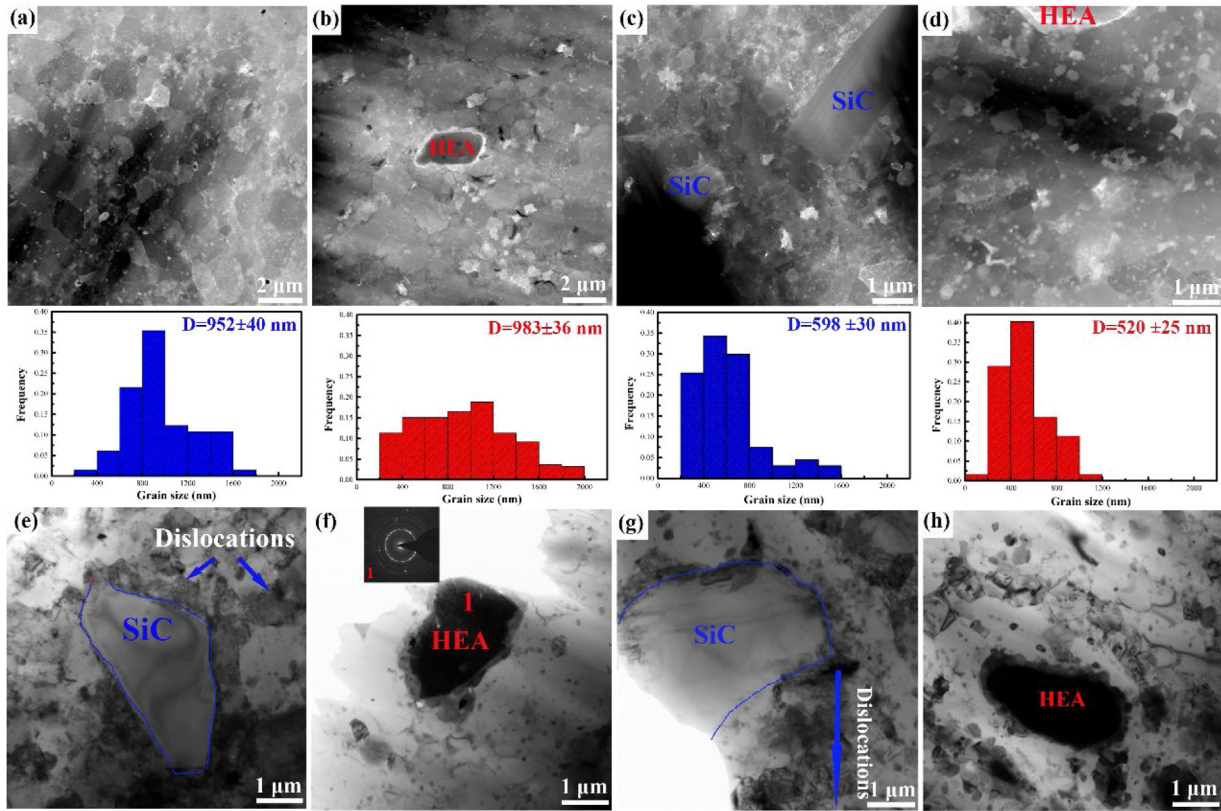
Fig. 11 – TEM images about grains and interface conditions of composites: (a) and (e) 10SiC-2024Al composite, (b) and (f) 10HEA-2024Al composite, (c) and (g) 20SiC-2024Al composite, (d) and (h) 20HEA-2024Al composite.

[11,24]. Because of the relatively homogeneous microstructure, we select 10HEA-2024Al and 10HEA-2024Al composites as targets to study the difference in the strengthening mechanism. There is a difference of 29.8 MPa in the yield strength between 10HEA-2024Al and 10HEA-2024Al composites. According to the calculation formula for strengthening mechanisms [4], when the reinforcement particle size, volume fraction and grain size are nearly equal, the strength increments from Hall–Petch strengthening, load transfer effect and Orowan strengthening should show no obvious difference. Therefore, the difference in strength could only come from dislocation (GND) strengthening. It has been proposed by Ashby [26] that there are two possible sources of the GND strengthening. The first category is the CTE mismatch between the Al matrix and reinforcements induced GNDs when the composite cools down from the processing temperature. Another category is the geometrical mismatch, and it is a result of the deformation-induced plastic strain gradient that arises when the composite is plastically deformed. Based on the equations in the literature [16], the strengthening values from the geometrical mismatch for two composites are also nearly equal. Therefore, for 10HEA-2024Al and 10HEA-2024Al composites, the difference in strength is mainly reflected in the CTE mismatch between the Al matrix and reinforcements, calculated as [27]:

$$\Delta\sigma_{CTE} = \omega G_M b_M \sqrt{\rho_{GND}} \qquad (1)$$

$$\rho_{CTE} = \frac{12\Delta T \cdot \Delta\alpha \cdot f}{b_M d(1-f)} \qquad (2)$$

where ω is the a constant of 1.25 [28], and ρ_{GND} is the density of GNDs; G_M and b_M are the shear modulus and Burgers vector of the Al matrix, respectively; d and f are the radius and volume fraction of reinforcements. $\Delta\alpha$ is the difference in the coefficient of thermal expansion (CTE) between the Al matrix and the reinforcements, $CTE_{Al} = 22.8 \times 10^{-6}/^\circ C$, $CTE_{SiC} = 4.7 \times 10^{-6}/^\circ C$ and $CTE_{HEA} = 14.7 \times 10^{-6}/^\circ C$ [16,20]. Finally, the strength of the 10HEA-2024Al and 10HEA-2024Al composites from the the CTE mismatch are 15.3 MPa and 21.4 MPa, respectively, which is the biggest difference in the strength increment in the two composites in comparison with other strength mechanisms [26–28].

Taya et al. [29] proposing when the thermal stress exceeded the yield strength of the matrix, the dislocation loops near the interface are punched out into the matrix with a punching distance to relax the thermal stress and then form a dislocation punched zone in the matrix. The nanoindentation results show that for the 10SiC-2024Al and 10HEA-2024Al composites, the width of hardness transition region is ∼3 μm and ∼2 μm, respectively. Next, the calculation and the simulation are used to compare the length of dislocation punched zones between both composites. The Eqs. (3)–(5) are usually utilized to calculate the length of dislocation punched
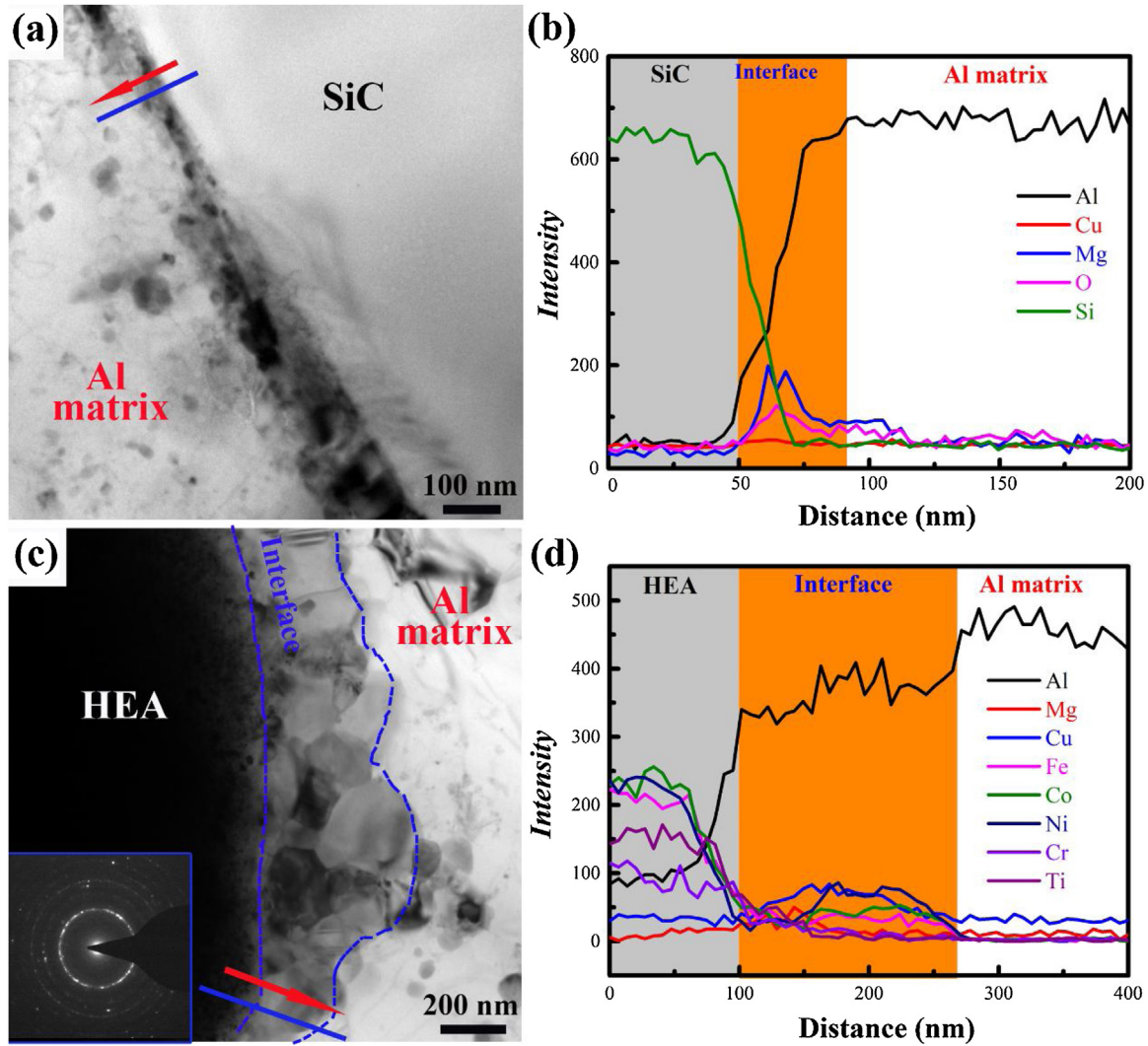
Fig. 12 – The interface between the Al matrix and reinforcements in 10SiC-2024Al and 10HEA-2024Al composites: the bright-filed image of the interface in the 10SiC-2024Al (a) and 10SiC-2024Al (c) composites, element distribution along the linear scanning of SiC/Al (b) and HEA/Al (d) interfaces.

zones [11,30].

$$a = d \left\{ \left(\frac{B(1-2Pf) + \sqrt{B^2(1-2Pf)^2 + 16\left(\tau_{ym}/G_m\right)PB}}{4\left(\tau_{ym}/G_m\right)} \right)^{\frac{1}{3}} - 1 \right\} \tag{3}$$

$$B = \frac{(1+\gamma_m) \cdot \Delta CTE \cdot \Delta T}{(1-\gamma_m)} \tag{4}$$

$$P = \frac{2(1-\gamma_m)(3\Delta\lambda + 2\Delta G)}{(1-\gamma_m)\left\{(1-f)(3\Delta\lambda + 2\Delta G) + 3[f(3\lambda_p + 2G_p)\left(\frac{1+\gamma_m}{1-\gamma_m}\right) + (1-f)(3\lambda_m + 2G_m)]\right\}} \tag{5}$$

Here, subscripts "m" and "p" stand for the matrix and particle, respectively. In Eqs. (3)–(5), ΔCTE is the difference in the CTE between the matrix and the particle, ΔT is the temperature change, τ_{ym} is the shear yield strength of the matrix, which

can be identified as the frictional stress for the glide motion of dislocations, and is assumed to be constant without considering the work hardening effect [9], λ and G is the Young modulus and shear modulus, γ_m is the Poisson's ratio, and $\Delta\lambda = \lambda_p - \lambda_m$ and $\Delta G = G_p - G_m$ are the mismatch of the Lame constants [30]. Finally, the length of dislocation punched zones for 10SiC-2024Al and 10HEA-2024Al composites are calculated to ~8 μm and ~5 μm, which are notably larger than results of the nanoindentation tests.

Finite element model (FEM) has been a common method to evaluate the deformation mechanism and residual thermal stress [31–33]. FEM was used here to evaluate the dislocation punched zone in the thermal residual stress of two composites during the cooling process using ANSYS Workbench 15
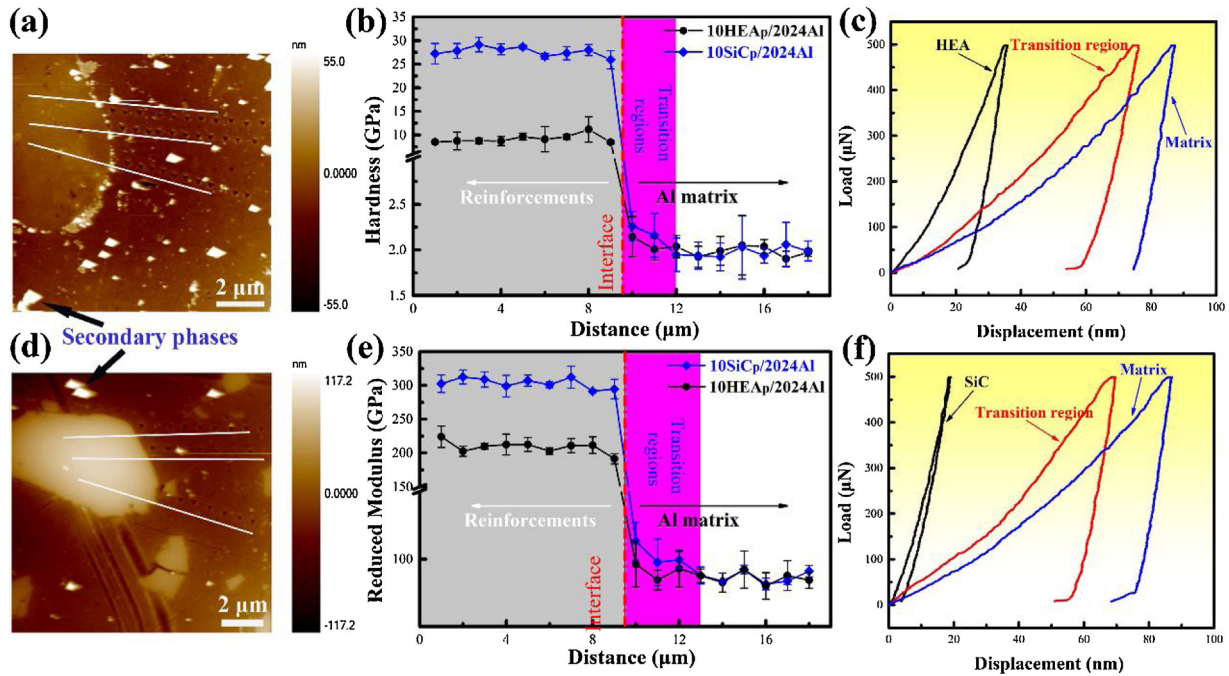
Fig. 13 – Variation of indentation hardness and reduced modulus along the particle-matrix interfaces in the 10SiC-2024Al and 10HEA-2024Al composites: (a) and (d) optical images of 10SiC-2024Al and 10HEA-2024Al composites, (b) variation of hardness, (e) variation of reduced modulus, (c) and (f) typical P–h curves of the reinforcement, transition region and matrix in 10SiC-2024Al and 10HEA-2024Al composites.

software and a thermo-mechanical coupled model. The simulation results in Fig. 14(a) and (b) qualitatively show the stress distribution surrounding various particulates. We assume that both composites have the homogenous microstructure and same particle size, and the simulation models of 10SiC-2024Al and 10HEA-2024Al composites are simplified as Fig. 14(c). Three features in two composites are directly observed as follows: (i) the thermal stress concentration takes place at the interface between the Al matrix and reinforcements, (ii) the thickness of the stress zone surrounding a circle particle is proportional to the particle size, (iii) most important of all, the stress value in the 10SiC-2024Al composite is near two times than that of the 10HEA-2024Al composite. A line showing stress distribution across the interface from the Al matrix towards the reinforcements are presented in Fig. 14(d), the length with the large stress fluctuation which can be regarded as the dislocation punched zones in 10SiC-2024Al and 10SiC-2024Al composites are ~5 μm and ~4 μm. The variation of hardness is not obvious in the dislocation punched zone away from the interface, which is the reason that the length of the dislocation punched zone measured by nanoindentation tests is obviously lower than theoretical and numerical simulated values. Nonetheless, the tendency is consistent in three methods. It is worth mentioning that the residual thermal stress in SiC particles is significantly higher than that of HEA particles, as shown in Fig. 14(c) and (d), which is also related with the condition that the SiC particles were mostly fractured in the 10SiC-2024Al composite, and the HEA particles only show

interface debonding in the 10HEA-2024Al composite. Shortly, the difference in the dislocation punched zones is the decisive reason for the fracture mechanism and strengthening effect of the two composites.

To describe the comprehensive comparisons between SiC-2024Al and HEA-2024Al composites, a schematic radar chart is presented in Fig. 15. We take the 10SiC-2024Al and 10HEA-2024Al composites for example. The mechanical properties of two composites are presented numerically, while the value of microstructure homogeneity, interfacial bonding and machinability are not quantitative and mainly deduced from SEM and TEM observation and turning experiments. Seen from Fig. 15, the 10 HEA-2024Al composite shows better overall performance than that of the 10SiC-2024Al composite. When the volume fraction of reinforcements increase, the advantage in microstructure homogeneity and machinability will be more obvious. The parameters of NC-HEA reinforcements (particle size, the density, etc.) and interface diffusion degree are not optimized yet, and it is believed that the mechanical properties of the HEA/Al composites could be further improved when these parameters reach optimal value. Another problem is the high cost and complex preparation process of nanocrystalline high-entropy alloy particles, which will be improved in the future work. In other filed, such as wear-resistant and electronic packaging industries, the SiC-2024Al composites maybe show better properties. In a word, above results and discussions provide some experience to design composites for different structural applications.
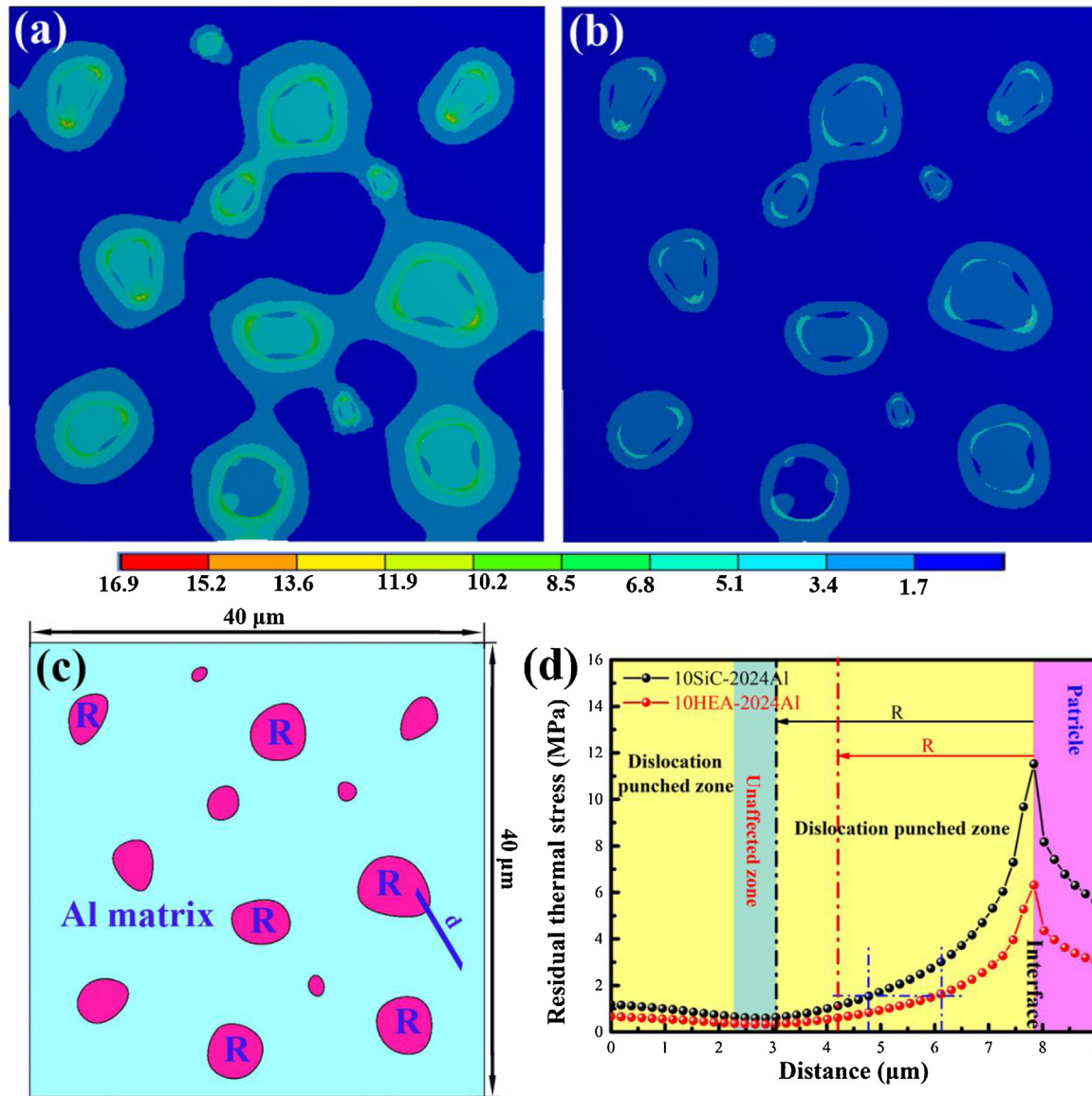
Fig. 14 – Finite element analysis used to evaluate the residual thermal stress of composites: (a) stress field of the 10SiC-2024Al composites, (b) stress field of the 10HEA-2024Al composites, (c) the model used in the finite element analysis, (d) the stress distributed along the matrix-reinforcement interface, the line marked in (c).

5. Conclusion

In this study, microstructure, mechanical properties and machinability of SiC particulate reinforced 2024Al and NC-HEA particulate reinforced 2024Al composites are systematically studied. In terms of microstructure, when the volume fraction of reinforcements is 10%, the SiC-2024Al and HEA-2024Al composites show a uniform particle distribution in the matrix. With increasing the reinforcement content, HEA-2024Al composites show denser microstructure than those of SiC-2024Al composites. The HEA-2024Al composites show better plasticity than SiC-2024Al composites, which is related with interface bonding condition of two kinds of composites. However, the strength show the opposite results. The CTE mismatch between the Al matrix and reinforcements is the decisive factor for the difference in the strength of the two composites. Last but not least, the HEA-2024Al composites show better hot-workability and turning performance than those of the SiC-2024Al composites. Above all, the reinforcement type is an important parameters to design the composites for structural applications.
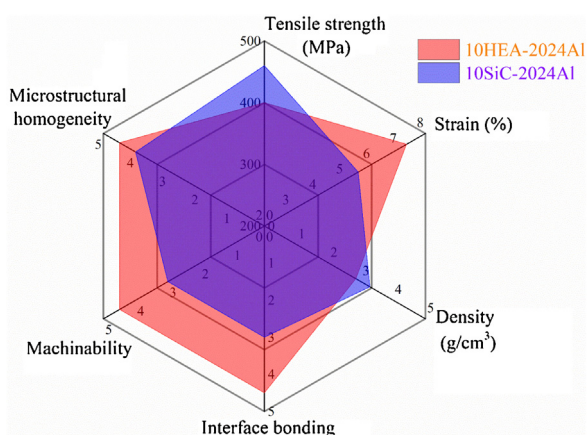
Fig. 15 – Radar chart of comprehensive comparisons between two kinds of composites, taking the 10SiC-2024Al and 10HEA-2024Al composites for example.

Conflicts of interest

The author declares no conflicts of interest.

Acknowledgments

REFERENCES

[1] Ni D, Wang J, Zhou Z, Ma Z. Fabrication and mechanical properties of bulk NiTi$_p$/Al composites prepared by friction stir processing. J Alloy Compd 2014;586:368–74.

[2] Suryanarayana C, Al-Aqeeli N. Mechanically alloyed nanocomposites. Prog Mater Sci 2013;58(4):383–502.

[3] Ma X, Zhao Y, Tian W, Qian Z, Chen H, Wu Y, et al. A novel Al matrix composite reinforced by nano-AlNp network. Sci Rep 2016;6:34919.

[4] Li Y, Liu W, Ortalan V, Li W, Zhang Z, Vogt R, et al. HRTEM and EELS study of aluminum nitride in nanostructured Al 5083/B$_4$C processed via cryomilling. Acta Mater 2010;58(5):1732–40.

[5] Yang H, Jiang L, Balog M, Krizik P, Schoenung J. Reinforcement size dependence of load bearing capacity in ultrafine-grained metal matrix composites. Metall Mater Trans A 2017;48(9):4385–92.

[6] Bai W, Roy A, Sun R, Silberschmidt V. Enhanced machinability of SiC-reinforced metal-matrix composite with hybrid turning. J Mater Process Technol 2019;268:149–61.

[7] Bhushan R, Kumar S, Das S. Effect of machining parameters on surface roughness and tool wear for 7075 Al alloy SiC composite. Int J Adv Manuf Technol 2010;50(5–8):459–69.

[8] Ozben T, Kilickap E, Cakır O. Investigation of mechanical and machinability properties of SiC particle reinforced Al-MMC. J Mater Process Technol 2008;198:220–5.

[9] Sekhar R, Singh T. Mechanisms in turning of metal matrix composites: a review. J Mater Res Technol 2015;4:197–207.

[10] Dong S, Zhou J, Hui D, Wang Y, Zhang S. Size dependent strengthening mechanisms in carbon nanotube reinforced metal matrix composites. Compos A Appl Sci Manuf 2015;68:356–64.

[11] Shao J, Xiao B, Wang Q, Ma Z, Yang K. An enhanced FEM model for particle size dependent flow strengthening and interface damage in particle reinforced metal matrix composites. Compos Sci Technol 2011;71(1):39–45.

[12] Wang G, Zuo L. Strengthening mechanism of load sharing of particulate reinforcements in a metal matrix composite. J Mater Sci 2007;42(12):4215–26.

[13] Meng G, Lin X, Xie H, Yue T, Ding X, Sun L, et al. The effect of Cu rejection in laser forming of AlCoCrCuFeNi/Mg composite coating. Mater Des 2016;108:157–67.

[14] Yang X, Dong P, Yan Z, Cheng B, Zhai X, Chen H, et al. AlCoCrFeNi high-entropy alloy particle reinforced 5083Al matrix composites with fine grain structure fabricated by submerged friction stir processing. J Alloy Compd 2020;836:155411.

[15] Lu T, Chen W, Li Z, He T, Li B, Li R, et al. Processing and mechanical properties of fine grained Al matrix composites reinforced with a uniform dispersion of nanocrystalline high-entropy alloy particles. J Alloy Compd 2019;801:473–7.

[16] Chen W, Li Z, Lu T, He T, Li R, Li B, et al. Effect of ball milling on microstructure and mechanical properties of 6061Al matrix composites reinforced with high-entropy alloy particles. Mater Sci Eng A 2019;762:138116.

[17] Selvakumar S, Dinaharan I, Palanivel R, Ganesh Babu B. Characterization of molybdenum particles reinforced Al6082 aluminum matrix composites with improved ductility produced using friction stir processing. Mater Charact 2017;125:13–22.

[18] Thangarasu A, Murugan N, Dinaharan I, Vijay S. Synthesis and characterization of titanium carbide particulate reinforced AA6082 aluminium alloy composites via friction stir processing. Arch Civ Mech Eng 2015;15:324–34.

[19] Jin P, Xiao BL, Wang QZ, Ma ZY, Liu Y, Li S. Effect of solution temperature on aging behavior and properties of SiC$_p$/Al-Cu-Mg composites. Mater Sci Eng A 2011;528(3):1504–11.

[20] Lu T, Scudino S, Chen W, Wang W, Li D, Mao M, et al. The influence of nanocrystalline CoNiFeAl$_{0.4}$Ti$_{0.6}$Cr$_{0.5}$ high-entropy alloy particles addition on microstructure and mechanical properties of SiC$_p$/7075Al composites. Mater Sci Eng A 2018;726:126–36.

[21] Liu Y, Yang C, Chen W, Zhu D, Li Y. Effects of particle size and properties on the microstructures, mechanical properties, and fracture mechanisms of 7075Al hybrid composites prepared by squeeze casting. J Mater Sci 2014;49(22):7855–63.

[22] Dabade U, Joshi S. Analysis of chip formation mechanism in machining of Al/SiC$_p$ metal matrix composites. J Mater Process Technol 2009;209:4704–10.

[23] Oliver W, Pharr G. An improved technique for determining hardness and elastic modulus using load and displacement sensing indentation experiments. J Mater Res 2011;7(6):1564–83.

[24] Guo X, Guo Q, Nie J, Liu Z, Li Z, Fan G, et al. Particle size effect on the interfacial properties of SiC particle-reinforced Al-Cu-Mg composites. Mater Sci Eng A 2018;711:643–9.

[25] Song J, Guo Q, Ouyang Q, Su Y, Zhang J, Lavernia E, et al. Influence of interfaces on the mechanical behavior of SiC particulate-reinforced Al-Zn-Mg-Cu composites. Mater Sci Eng A 2015;644:79–84.

[26] Ashby M. The deformation of plasticity non-homogeneous materials. Philos Mag 1970;21:399–424.

[27] Zhang Z, Topping T, Li Y, Vogt R, Zhou Y, Haines C, et al. Mechanical behavior of ultrafine-grained Al composites

reinforced with B4C nanoparticles. Scr Mater 2011;65(8):652–5.

[28] Jiang L, Yang H, Yee J, Mo X, Topping T, Lavernia E, et al. Toughening of aluminum matrix nanocomposites via spatial arrays of boron carbide spherical nanoparticles. Acta Mater 2016;103:128–40.

[29] Taya M, Lulay K, Lloyd D. Strengthening of a particulate metal matrix composite by quenching. Acta Metall Mater 1991;39:73–87.

[30] Lin K, Pang S. The influence of thermal residual stresses and thermal generated dislocation on the mechanical response of particulate-reinforced metal matrix nanocomposites. Compos B Eng 2015;83:105–16.

[31] Liu L, Yang C, Zhang W, Xiao Z, Zhang L. Correlation between microstructure and deformation mechanism in $Ti_{66}Nb_{13}Cu_8Ni_{6.8}Al_{6.2}$ composites at ambient and elevated temperatures. Mater Sci Eng A 2019;767:138448.

[32] Węglewski W, Michał B, Marcin C, Katarzyna P. Modeling of thermally induced damage in the processing of $Cr-Al_2O_3$ composites. Compos B Eng 2012;43(2):255–64.

[33] Bao Y, Liu C, Huang J. Effects of residual stresses on strength and toughness of particle-reinforced TiN/Si_3N_4 composite: theoretical investigation and FEM simulation. Mater Sci Eng A 2006;434(1–2):250–8.